Oxidation State and Symmetry of Magnesia-Supported $Pd_{13}O_x$ Nanocatalysts Influence Activation Barriers of CO Oxidation

Michael Moseler,*[,†,‡] Michael Walter,[†,‡] Bokwon Yoon,[§] Uzi Landman,[§] Vahideh Habibpour,[‖] Chris Harding,[‖] Sebastian Kunz,[‖] and Ueli Heiz[‖]

[†]Freiburg Materials Research Center, University of Freiburg, Stefan-Meier-Strasse 21, 79104 Freiburg, Germany
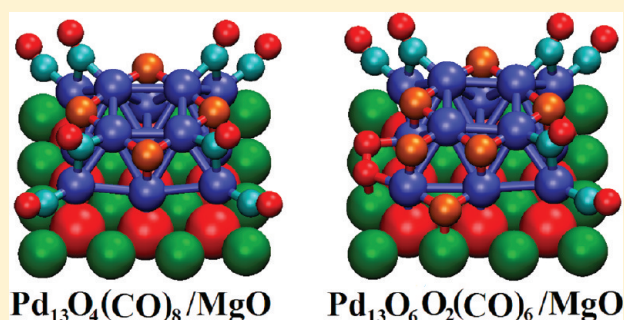[‡]Fraunhofer Institute for Mechanics of Materials IWM, Wöhlerstrasse 11, 79108 Freiburg, Germany
[§]School of Physics, Georgia Institute of Technology, Atlanta, Georgia 30332-0430, United States
[‖]Lehrstuhl für Physikalische Chemie, Technische Universität München, Lichtenbergstrasse 4, 85748 Garching, Germany

S Supporting Information

ABSTRACT: Combining temperature-programmed reaction measurements, isotopic labeling experiments, and first-principles spin density functional theory, the dependence of the reaction temperature of catalyzed carbon monoxide oxidation on the oxidation state of Pd_{13} clusters deposited on MgO surfaces grown on Mo(100) is explored. It is shown that molecular oxygen dissociates easily on the supported Pd_{13} cluster, leading to facile partial oxidation to form $Pd_{13}O_4$ clusters with C_{4v} symmetry. Increasing the oxidation temperature to 370 K results in nonsymmetric $Pd_{13}O_6$ clusters. The higher symmetry, partially oxidized cluster is characterized by a relatively high activation energy for catalyzed combustion of the first CO molecule via a

reaction of an adsorbed CO molecule with one of the oxygen atoms of the $Pd_{13}O_4$ cluster. Subsequent reactions on the resulting lower-symmetry $Pd_{13}O_x$ ($x < 4$) clusters entail lower activation energies. The nonsymmetric $Pd_{13}O_6$ clusters show lower temperature-catalyzed CO combustion, already starting at cryogenic temperature.

I. INTRODUCTION

Although many industrial catalytic processes take place on metal nanoparticles that are oxidized during the reaction, a detailed knowledge of the influence of the oxidation state on their catalytic activity is still lacking (see ref 1 for a recent review). For instance, a large number of publications reporting on fundamental investigations about the chemical and catalytic properties have appeared for palladium (one of the metals often used in catalysis[2]), particularly because of the importance of Pd-catalyzed oxidation reactions in the automotive industry,[3] and the environmental interest in efficient, low-temperature, catalyzed combustion of noxious exhaust gases.[4] However, the importance of intermediate surface oxide phases in catalytic reactions involving palladium has been recognized only recently.[5] This work was followed by studies pertaining to the nature of different oxygen species on palladium surfaces,[6] as well as their interaction with reactants such as CO under UHV as well as ambient pressure conditions.[7,8] In a systematic experimental study,[9] it was found that the type of palladium surface oxide may be the determining factor governing the catalytic action, and that the chemisorbed oxygen serves as the most reactive species, because a layer of chemisorbed oxygen atoms, O(ad), is able to coadsorb CO(ad).

For Pd nanoparticles on metal oxide surfaces, the presence of the support, the finite size of the particles, and the particle size

dispersion add significant complexity to the oxide formation. Molecular beam experiments with 4−10 nm Pd particles on Fe_3O_4 at $T = 500$ K suggest the formation of a Pd oxide at the particle/support interface and the chemisorption of oxygen on the metallic upper part of the nanoparticles.[10] Both oxygen species contribute to the CO combustion. The same study deduced for Pd particles with diameters smaller than 3 nm complete oxidation to PdO at high temperatures. This finding is in line with high-energy X-ray studies of the size-dependent $T = 500$ K oxidation of Pd nanoparticles on MgO(100).[11]

Apart from a density functional study predicting the easy transformation of small, noncrystalline, magnesia-supported Pd-clusters to crystalline Pd_xO_y nanooxides,[12,13] the role of oxides in the low-temperature heterogeneous catalysis of small Pd nanoclusters is unexplored.

Here, we show that the oxidation state of Pd_{13} clusters supported on magnesia plays an important role in the Pd-catalyzed oxidation of CO: a $T = 370$ K pretreatment by molecular oxygen significantly lowers the temperature for CO_2 formation in our temperature-programmed-reaction (TPR) experiments. Through the correlation of first-principles computational modeling with the TPR data, we find that

cryogenic O_2 treatment produces highly symmetric $Pd_{13}O_4$ clusters while asymmetric $Pd_{13}O_6$ forms when exposed to O_2 at 370 K. In our simulations, the spectrum of activation energies for reaction steps along the reaction pathways depends on the overall symmetry of the cluster–reactants complex. Highly symmetric structures of the cluster/reactant complex increase the activation energy of the catalytic reaction steps, whereas asymmetric cluster/reactant structures can accelerate the process. The reduced activation energy is related to the breaking of local charge and orbital symmetry, resulting in stronger bonding of atomic oxygen to one of the Pd atoms and promoting the reaction with a CO sharing this Pd atom.

II. METHODS

Experiment. The model catalysts were prepared by depositing size-selected metal clusters with low kinetic energy (1 eV/atom) onto well-defined MgO films.[14,15] For each cluster deposition experiment, the magnesium oxide films were prepared in situ by epitaxial growth onto a Mo(100) single crystal.[16] The thicknesses of the films were typically around 10 monolayers; $^{16}O_2$ partial pressure, evaporation rate, and growth temperature were 5×10^{-7} mbar, 0.1 ML min^{-1}, and 320 K, respectively. Auger electron spectroscopy (AES), metastable helium impact electron spectroscopy (MIES), and ultraviolet photo-electron spectroscopy (UPS) were employed to verify the cleanliness and characterize the electronic states of the oxide layer. The Pd_{13} clusters were produced using a high frequency (120 Hz) laser vaporization source.[17] The cluster beam was guided by a set of ion optics through differentially pumped vacuum chambers, where the positively charged clusters were deflected by a custom-made, electrostatic ion bender and focused into a quadrupole mass-selecting unit (ABB-Extrel; mass limit 4000 amu). The mass-selected Pd_{13} cluster beam is further guided by a set of Einzel lenses and finally soft-landed onto the MgO surface. Neutralization of the clusters upon deposition either occurs at surface defects or via charge tunneling through the thin films.[18,19] Cluster coverage was less than 0.2% of a monolayer (1 ML $\approx 2.25 \times 10^{15}$ clusters cm^{-2}) as measured from the integration of the cluster current during deposition. This ensures the supported clusters to be well isolated; furthermore, substrate temperatures of around 100 K prevent agglomeration.

After deposition, two types of experiments were performed. For the first type, the reactivity of the size-selected Pd_{13} clusters was measured directly after deposition. In the second type, prior to the reactivity studies the supported clusters were oxidized by annealing them at a given temperature (~370 K) in an oxygen background of 5×10^{-7} mbar for 1 min. The catalytic performance of both the virginal and the oxidized Pd clusters was then explored using temperature-programmed reaction (TPR) and isotopic labeling experiments. In these experiments, a differentially pumped quadrupole mass spectrometer (Balzers QMG 421) was used to detect the product molecules formed on the model catalyst, while the temperature of the sample was linearly increased at a constant rate (~2 K/s). To further study the CO combustion on the Pd clusters, infrared measurements of adsorbed carbon monoxide were accomplished by means of a commercial Fourier transform infrared (FTIR) spectrometer (Thermo Nicolet 6700). The IR radiation was focused onto the sample at grazing incidence with the use of a concave IR-mirror. The reflected IR radiation was detected with a liquid nitrogen-cooled MCT detector (EG&G Optoelectronics). In all measurements, the ^{13}CO isotopomer was used as a probe molecule to enhance the signal-to-noise ratio of the measurements. FTIR spectra were recorded over 512 scans with a resolution of 4 cm^{-1}.

Theory. The electronic structure of the Pd_{13} clusters supported by MgO was described using spin density functional theory, calculated with the grid-projector-augmented-wave (GPAW) method.[20,21] A grid-spacing of 0.2 Å was used for the configuration space grid representation of the smooth wave functions. Dirichlet boundary conditions were applied for gas-phase molecules. For the supported cluster model, periodic boundary conditions were applied in the surface plane and Dirichlet boundary conditions perpendicular to the surface. Only the Γ-point was considered for the periodic wave functions.

The exchange-correlation energy was described in the generalized-gradient-approximation (GGA) as devised by Perdew, Burke, and Ernzerhof (PBE),[22] and the results were cross-checked using the meta-GGA approach of Tao et al (TPSS),[23] because PBE has a well-known problem with the atomization energy of the gasphase O_2 molecule.[24] While PBE overestimates it by 1 eV, our TPSS result of 5.35 eV comes close to the experimental estimate of 5.23 eV.[24] PBE structural and energetic information is reported throughout this Article. Because dissociation of O_2 on the supported Pd_{13} cluster will be considered in this Article, all PBE energy differences (e.g., dissociation energies) are accompanied by corresponding post TPSS values in square brackets. As will become evident for the majority of systems and reactions considered in this Article, PBE and TPSS results are in good agreement. In the rare cases where larger deviations occur, the results from both functionals lead to the same conclusions.

The MgO film was modeled by a three-layer rock-salt structure MgO(001) film at the experimental lattice constant of 4.21 Å in a periodic (5×5) surface cell. The two lowest MgO layers were held fixed during geometry optimization using the FIRE algorithm.[25] All structures were assumed to be relaxed when the forces were smaller than 0.05 eV/ Å. Convergence with respect to supercell size was checked by additional calculations of a fully CO and O_2 saturated Pd_{13} nanooxide on a MgO slab with (6×6) periodicity. All admolecule binding energies deviated not more than 0.05 eV from the (5×5) results reported in this Article.

The minimum energy pathways and barriers of the O_2 dissociation reactions were calculated employing the nudged elastic-band method[26] in combination with the climbing image algorithm[27] for the transition state. Typically 8−16 images along the reaction path were used. The CO+O reaction pathways were obtained by constrained energy minimization for a set of fixed distances between the carbon and the reacting oxygen on the nano-oxide. All reaction pathways were calculated using spin-paired PBE calculations. Their corresponding energetics (in particular, the barrier height) was determined within a post spin-polarized PBE and TPSS calculation by minimizing the total energy of each image with respect to the z-component of the spin. Such a mixed procedure can be motivated by the observed insensitivity of the reaction pathways to the applied functional;[28] that is, differences between the spin-paired and spin-polarized pathways are small, while the barrier heights from a spin-polarized calculation might significantly deviate from the corresponding spin-paired one.

III. RESULTS

Experiment. Figure 1 depicts temperature-programmed reaction (TPR) spectra of carbon dioxide produced at size-selected Pd_{13} clusters supported on a magnesia, MgO(001), surface, under two different experimental conditions. In the first (type I) experiment, the Pd_{13} cluster samples (as prepared) were exposed to oxygen ($^{16}O_2$) and carbon monoxide (^{13}CO) at 120 K prior to the TPR experiment. In the second (type II) experiment, the Pd_{13} clusters were first oxidized at 370 K in an oxygen, $^{16}O_2$, background of 5×10^{-7} mbar, and after being cooled to cryogenic temperatures, the $Pd_{13}{}^{16}O_x$ cluster samples were exposed to $^{16}O_2$ and subsequently to ^{13}CO. In the type I experiment, a broad peak around 400 K is observed as shown in the upper spectrum of Figure 1, whereas for the oxidized Pd_{13} clusters three different reaction channels can clearly be distinguished (see middle spectrum of Figure 1), in which carbon dioxide ($^{13}C^{16}O_2$) is formed at around 200, 300, and 400 K and which are labeled with α, β, and γ, respectively. The α-mechanism is clearly less efficient than the other two mechanisms when the model catalyst was exposed to the two reactant molecules at 120 K.
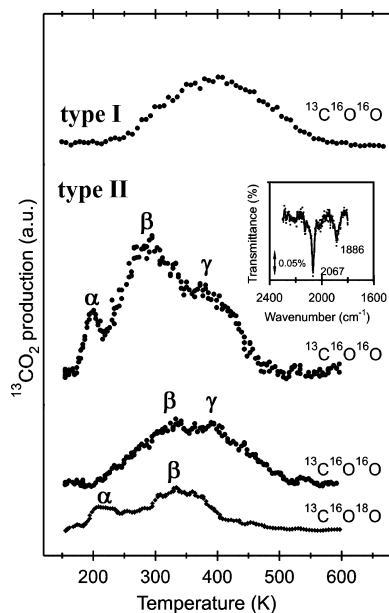
7691

dx.doi.org/10.1021/ja211121m | J. Am. Chem. Soc. 2012, 134, 7690−7699

Figure 1. Upper spectrum: $^{13}C^{16}O_2$ formation on magnesia-supported $Pd_{13}(\sim0.17\%ML)$. The clusters were deposited and subsequently exposed to $^{16}O_2$ and $^{13}C^{16}O$. Middle spectrum: TPR spectra of $^{13}C^{16}O_2$ formation on magnesia-supported palladium oxide clusters ($Pd_{13}{}^{16}O_x$, $\sim0.17\%ML$). The Pd_{13} clusters were oxidized at ~370 K in $^{16}O_2$ atmosphere, and the temperature ramp was performed after $^{16}O_2$ and $^{13}C^{16}O$ exposure at ~120 K. Lower two spectra: TPR spectra of $^{13}C^{16}O^{16}O$ and $^{13}C^{16}O^{18}O$ formation on magnesia-supported palladium oxide clusters ($Pd_{13}{}^{16}O_x$, $\sim0.17\%ML$). The Pd_{13} clusters were oxidized at ~370 K in $^{16}O_2$ atmosphere, and the temperature ramp was performed after $^{18}O_2$ and $^{13}C^{16}O$ exposure at ~120 K. The oxidation products are shown with "●" ($^{13}C^{16}O^{16}O$ upper curve) and "◆" ($^{13}C^{16}O^{18}O$ lower curve) markers. (Inset) IR spectra of adsorbed ^{13}CO on $Pd_{13}O_x$ clusters supported on a MgO film. For the measurements presented, a background spectrum (CO free) was subtracted.

For both types of experiments, displayed in Figure 1, one may inquire about the stage of the reaction process when oxygen dissociates at the cluster surface, and to what extent the oxidized palladium clusters serve in the course of the reaction as a source of oxygen for the combustion of CO. Moreover, one may also explore whether the oxygen used for dosing the system at cryogenic temperature participates in the oxidation reaction altogether. To obtain details about the reaction mechanisms, isotopic labeling experiments were performed for the type II experiment. Typical results of such experiments are shown in the two lowest spectra of Figure 1 for the combustion of CO on a model catalyst of oxidized Pd_{13} ($Pd_{13}{}^{16}O_x$ 0.17% ML). In these experiments, the Pd clusters were oxidized at 370 K in a $^{16}O_2$ background ($p_{oxygen} = 5 \times 10^{-7}$ mbar).

After the sample was cooled to 120 K and the residual $^{16}O_2$ was pumped out of the system, the catalyst was sequentially exposed to $^{18}O_2$ and $^{13}C^{16}O$. Two isotopomers, $^{13}C^{16}O^{16}O$ and $^{13}C^{16}O^{18}O$, were detected by a mass spectrometer during a temperature ramp. The formation of $^{13}C^{16}O^{16}O$ can be described by a mechanism in which the oxygen of the oxidized cluster is involved. In contrast, the other isotopomer ($^{13}C^{16}O^{18}O$) results from the oxidation of CO with the cryogenic oxygen. As depicted in Figure 1, the oxidized palladium clusters contribute to the formation of $^{13}C^{16}O^{16}O$ in

a broad temperature window of above 200 K to about 500 K. Two maxima in the desorption spectra are observed at 340 and 400 K (labeled β and γ in Figure 1). Interestingly, the contribution of the cryogenic $^{18}O_2$ is much smaller with two active reaction channels for the formation of $^{13}C^{18}O^{16}O$ at ~210 K (α-mechanism) and ~330 K (β-mechanism). From these results, it is evident that the α-mechanism originates solely from the presence of cryogenic (undissociated) oxygen, whereas the γ-mechanism results from the reduction of the (previously) oxidized palladium clusters, only. The β-mechanism is more complicated with less defined activation energies (broad temperature range); the isotopic scrambling suggests a dynamic exchange of the two different oxygen atoms on the cluster during reaction.

Further information about the model catalysts was obtained from Fourier transform infrared (FTIR) spectroscopy, measured prior to the reaction. The FTIR data are shown in the inset of Figure 1. The spectra were taken at 120 K after oxidation of the deposited Pd_{13} at ~370 K in an oxygen background of 5×10^{-7} mbar and saturating the model catalyst with $^{16}O_2$ and ^{13}CO at cryogenic temperature. The IR spectra exhibit a dominant and rather sharp vibrational band at 2068 cm^{-1} and a small feature at around 2000 cm^{-1}, as well as a relatively broad band at 1886 cm^{-1}. The latter two can clearly be attributed to CO bound to the $Pd_{13}O_x$ cluster where the high and low frequency bands are typical for on-top and bridge bound CO, respectively. It is unlikely that the sharp band at 2068 cm^{-1} originates from ^{13}CO adsorbed on the $Pd_{13}O_x$ cluster; we rather attribute this band to CO bound at the MgO substrate in the vicinity of the metal cluster. This is supported by the fact that upon heating the sample above 120 K this absorption peak immediately disappears, indicating a rather weak interaction of ^{13}CO with the model catalyst.

Theory. Carbon monoxide oxidation catalyzed by Pd_{13} clusters has been studied with the use of gradient-corrected spin-polarized density-functional-theory (DFT), aiming at understanding and elucidation of the reactions underlying the features in the TPR spectra obtained via the two (types I and II) experimental protocols described above. Models based on transmission electron microscopy experiments of magnesia (001)-supported Pd_N clusters predict octahedral shaped Pd clusters terminated by (111) facets and truncated at the top and at the Pd/MgO interface by (001) planes.[29] Indeed, we find a two-layer truncated square pyramid with 9 atoms in the first and 4 atoms in the second layer for the ground state of Pd_{13} supported by MgO (001); see structure I in Figure 2a for a side view (top left panel) and a top view (middle left panel). Interestingly, the four atoms square in the second adlayer of the cluster can deform to a rhombus, resulting in an isoenergetic isomer (structure II in the bottom panel of Figure 2a).

The interconversion between the two ground states I and II in Figure 2a is essentially barrierless, suggesting a flat basin of interpolating structures that coexist already at low temperatures. Both ground-state isomers are in a quintet state and 0.15 [0.35] eV lower in energy than a more compact three-layer structure (III in Figure 2a) with 5 atoms in the first adlayer as well as 3.66 [4.29] eV lower in energy than more flat isomer with all 13 atoms in the first adlayer (structure IV in Figure 2a). This suggests that our truncated square pyramid ground state represents a compromise between adhesion to the support and Pd–Pd cohesion.

Both supported Pd_{13} ground states are in a quintet spin state and bind to the MgO with an adsorption energy of 3.5 [3.9] eV
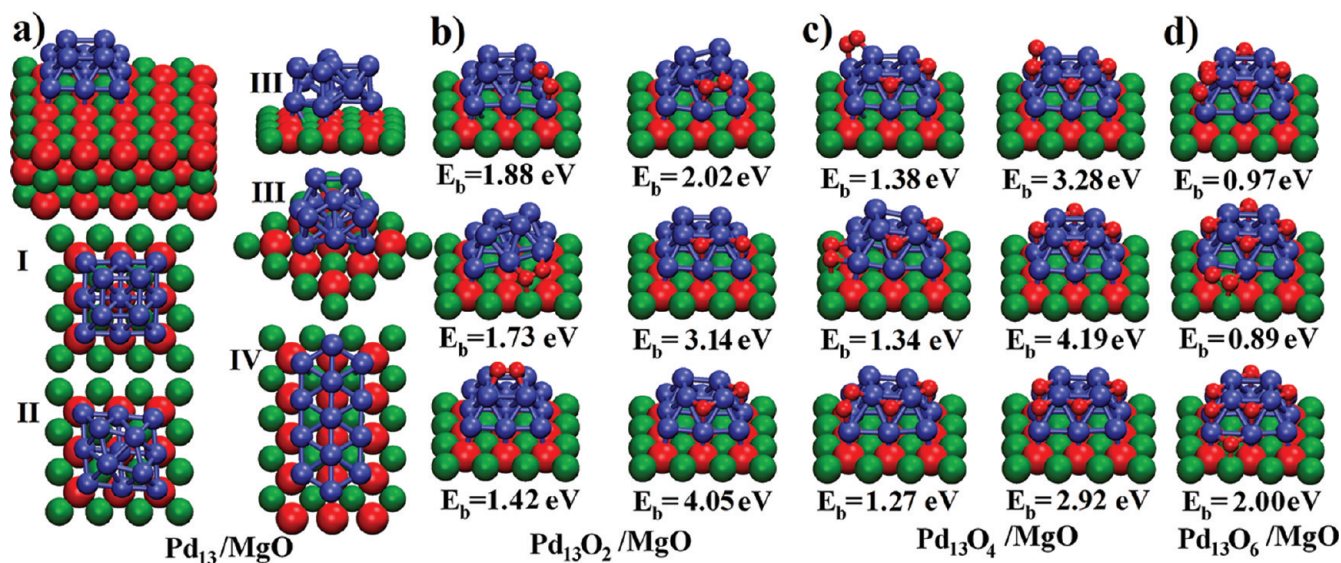
Figure 2. Oxidation mechanisms of magnesia-supported Pd_{13}. (a) Ground-state structure and energetically higher lying isomers of the Pd_{13} clusters after soft-landing. The top left panel displays a side view of the full system for the ground state. The three lowermost MgO layers are not shown in the following panels. The middle left panel (I) shows a top view of the C_{4v} ground state, while a C_{2v} distorted energetically degenerate isomer is shown in the bottom panel (II). The top right and middle right panels show the first higher isomer (III) from two different perspectives, and the bottom left panel (IV) displays a 13 atom monolayer structure on the MgO substrate. (b) Left column: Adsorption sites of a single oxygen molecule (shown from top to bottom) on a corner bridge ($E_b = 1.88$ eV), on top of Mg atoms ($E_b = 1.73$ eV), and on the Pd top square ($E_b = 1.42$ eV). Right column: The peroxo O_2 on a Pd side square ($E_b = 2.02$ eV), shown in the top row, dissociates with a barrier of 0.01 eV to form a nanooxide (middle row), with two atomic O on top of neighboring Pd atoms ($E_b = 3.14$ eV), which can evolve to the $Pd_{13}O_2$ ground state ($E_b = 4.05$ eV), shown at the bottom row, via a 0.1 eV barrier. (c) Left column: A second O_2 dimer can attach to corner bridge sites ($E_b = 1.38$ eV and $E_b = 1.27$ eV, shown at the top and bottom rows, respectively) or on top of Mg sites ($E_b = 1.34$ eV, shown at the middle row). Bottom row: The bridge-bonded O_2 can dissociate via barriers of the order 0.3 eV, crossing again peroxo states, into a metastable nanooxide ($E_b = 3.28$ eV and $E_b = 2.92$ eV in the sixth colunn). The $E_b = 3.28$ eV structure (top row) transforms easily (barrier 0.1 eV) into a C_{4v} $Pd_{13}O_4$ ground state with $E_b = 4.19$ eV (middle row), while the $E_b = 2.92$ eV structure (bottom row) has to cross barriers of the order 0.8 eV to isomerize into the ground state. (d) The third O_2 binds to a corner bridge ($E_b = 0.97$ eV, top row) or an Mg site ($E_b = 0.89$ eV, middle row) and dissociates (barrier 0.8 eV) in both cases to a $Pd_{13}O_6$ nanooxide ($E_b = 2.00$ eV, bottom row) with the two atomic O atoms on a corner bridge and on an Mg site. Color code: Mg atoms in green, oxygen in red (with adsorbed oxygen atoms depicted by the smaller spheres), and Pd atoms in blue.

relative to the nonet gas-phase Pd_{13} icosahedron.[30] A Bader charge analysis[31,32] reveals that approximately 0.10 and 0.08 electrons per Pd atom are transferred from the magnesia support to the first and second adlayer of the cluster, respectively.

Upon exposure to oxygen, the first O_2 molecule binds to the Pd_{13}/MgO preferentially at the following sites (ordered according to the binding energies): (i) at Pd–Pd corner bridges ($E_b = 1.88$ [1.89] eV; see Figure 2b); (ii) at the periphery of the cluster in a slightly tilted orientation above the Mg sites ($E_b = 1.73$ [1.71] eV, Figure 2b), and (iii) on top of the second adlayer Pd square ($E_b = 1.42$ [1.53] eV, Figure 2b). A strongly bound peroxo state on a Pd side square that forms after rhombic deformation of the second adlayer ($E_b = 2.02$ [2.11] eV, O_2 bond length $d = 1.53$ Å, Figure 2b) is accessible from the Pd–Pd corner bridge and the top square adsorption site via barriers of the order of 0.3 eV (0.32 [0.30] eV for bridge and 0.37 [0.29] eV for top square), and from the peripheral Mg adsorption site via a barrier of 0.65 [0.71] eV. From this peroxo state, the molecule dissociates with a negligible (0.01 [0.00] eV) barrier, resulting in two oxygen atoms, one on a corner bridge and the other at an edge hollow position ($E_b = 3.14$ [3.34] eV, Figure 2b); this configuration can relax further via a small barrier of 0.08 [0.05] eV into a Pd_{13}/MgO with two O on neighboring edge hollow positions ($E_b = 4.05$ [4.35] eV, Figure 2b) representing the $Pd_{13}O_2$/MgO ground-state structure. A similar situation occurs for the formation of $Pd_{13}O_4$/MgO. A

second dimer can adsorb to an opposite Pd–Pd corner bridge site ($E_b = 1.38$ [1.30] eV, Figure 2c) or on top of a Mg site ($E_b = 1.34$ [1.35] eV, Figure 2c) of the $Pd_{13}O_2$/MgO. The bridge bonded dimer dissociates via a barrier of 0.37 [0.39] eV into oxygen atoms, one on a corner bridge and the other at an edge hollow position ($E_b = 3.28$ [3.38] eV, Figure 2c). During dissociation, the O_2 passes again through a peroxo state (not shown). However, in this case, the peroxo state is not a stable minimum anymore (presumably because of the absence of a rhombus deformation of the Pd_4 square in the first adlayer).

The dissociation of the second O_2 is followed by migration of the O on the Pd_{13} corner bridge to the last vacant edge hollow site (barrier 0.14 [0.19] eV). This results in the highly symmetric C_{4v} $Pd_{13}O_4$/MgO cluster with an enhanced binding energy, E_b, of 4.19 [4.35] eV for the second dissociated oxygen molecule (Figure 2c). Its second adlayer Pd_4O_4 unit has already been found by one of us for magnesia-supported Pd_9 nanooxides.[12] Interestingly, it represents the basic building block of a Pd(111) surface oxide[5] and differs significantly from the $\sqrt{5} \times \sqrt{5}R27°$ surface oxide on Pd(100) whose stability has been predicted by Rogal et al. over a broad range of O_2 pressures.[7,8] Note, however, that the prediction in ref 8 is based on the assumption of thermodynamic equilibrium, while our experimental protocol (low-temperature dosing of O_2) suggests a kinetically determined nanooxide.

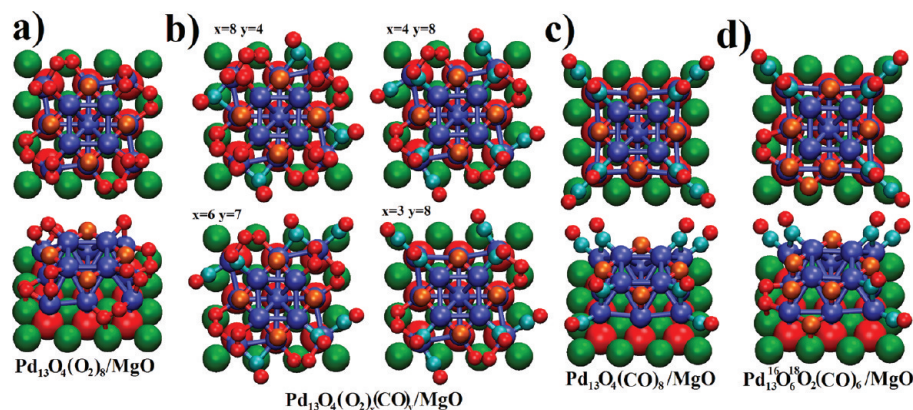The calculated adsorption energies and oxygen reaction barriers indicate that the particularly stable C_{4v} $Pd_{13}O_4$/MgO

Figure 3. Interaction of CO with the $Pd_{13}O_4$/MgO. Color code for Pd, Mg, and O as in Figure 2. Oxygen atoms of the $Pd_{13}O_4$ and $Pd_{13}O_6$ nano-oxides are highlighted in orange and C is shown as cyan spheres. (a) Full coverage of the $Pd_{13}O_4$ ground state with molecular oxygen. (b) CO adsorbs to Pd−Pd bridges above Mg sites (top left panel). Two O_2 molecules on opposite Pd corner bridges desorb clearing the corner bridge for the CO followed by adsorption of additional CO to first adlayer Pd corner atoms (bottom left panel) and the desorption of the remaining two O_2 on the corner bridges. After repopulation of the corner bridges with CO (top right panel), the CO on the Mg sites can move to the corner bridges accompanied by the desorption of the O_2 on the Mg sites (bottom right panel). (c) This results in a $Pd_{13}O_4$ ground state covered with 8 CO molecules. (d) Full coverage of the $Pd_{13}O_6$ core with 8 CO molecules and one molecular O_2.

ground state is very likely to form during O_2 exposure at relatively low temperatures. Note, however, that several other $Pd_{13}O_4$ nanooxides can be found that originate from energetically higher lying molecular adsorption configurations. For instance, adsorption of O_2 to another corner bridge site (E_b = 1.27 [1.23] eV, Figure 2c) followed by its dissociation results in an energetically higher lying $Pd_{13}O_4$ cluster (E_b = 2.92 [3.03] eV, Figure 2c) that can only be converted into the $Pd_{13}O_4$ nanooxides ground state (E_b = 4.19 [4.35] eV, Figure 2c) via a barrier of 0.79 [0.86] eV. Therefore, we assume that several nanooxide isomers might be present in the experiments whose relative weights depend on the experimental preparation conditions.

A third O_2 can bind to a vacant Pd−Pd corner bridge of the C_{4v} $Pd_{13}O_4$ ground state (E_b = 0.97 [0.95] eV, Figure 2d) or to Mg-sites (E_b = 0.89 [0.93] eV, Figure 2d). In both cases, dissociation of the O_2 proceeds via barriers of the order of 0.6−0.8 eV (0.82 [0.76] eV for the corner bridge and 0.60 [0.85] eV for the Mg-site) into atomic oxygen on a corner bridge and on a peripheral position on top of a Mg atom (E_b = 2.00 [2.18] eV, Figure 2d). The magnitudes of the barriers indicate that this third dissociation can only occur at elevated temperatures, suggesting that the C_{4v} $Pd_{13}O_4$/MgO nanooxide forms predominantly in the type I experiments, while less symmetric $Pd_{13}O_6$/MgO nanoxides are produced by the type II protocol. The $Pd_{13}O_6$/MgO can adsorb a fourth O_2 on a vacant corner bridge (E_b = 0.99 [0.94] eV, structure not shown). The dissociation barrier of this dimer (E_a = 0.98 [0.90] eV) is of the same order of magnitude as the desorption energy and because the prefactor in the Arrhenius expressions of the reaction rates is usually higher for desorption than for dissociation,[33] we consequently assume that the fourth dimer is likely to desorb from the cluster before dissociation.

In the type I experiment, oxygen dosing at cryogenic temperatures results in O_2 saturation of the cluster. Therefore, we explored in our density functional study the adsorption of additional O_2 molecules to the C_{4v} $Pd_{13}O_4$ nanooxide. The nanooxide binds four oxygen molecules on corner bridge sites and four O_2 molecules on Mg sites (near the Pd cluster periphery) with binding energies E_b = 0.62 [0.50] eV and E_b = 0.51 [0.44] eV, respectively (see Figure 3a). This represents the

maximum O_2 coverage, because further O_2 adsorption at the remaining four Mg sites turns out to be endothermic. Interestingly, the chiral arrangement of the adsorbed O_2 leads to a strong chiral distortion of the C_{4v} $Pd_{13}O_4$ core (Figure 3a).

It is not surprising that the empty Mg sites at the periphery of the cluster play a principal role in the CO attack following the CO dosing at 120 K. Coverage of these sites with CO molecules (top left panel of Figure 3b) results in the binding of CO with E_b = 0.52 [0.40] eV and a strong reduction of the binding energy of the O_2 on the corner bridges (E_b = 0.06 [0.13] eV). After immediate desorption of the first corner bridge O_2, the O_2 on the opposite corner bridge still shows weak binding (E_b = 0.16 [0.19] eV) and subsequently leaves the cluster. Even the remaining two O_2 on the corner bridges are destabilized upon repopulation of the vacant corner bridges and adsorption of additional CO on the first adlayer of the Pd_{13}. See, for instance, the additional CO molecule on the first adlayer Pd top position in the bottom left panel of Figure 3b that annihilates the binding of the neighboring O_2 molecule on the corner bridge (E_b = −0.15 [−0.19] eV). The same mechanism applies to the last O_2 on a corner bridge (E_b = −0.26 [−0.24] eV). Finally, the resulting $Pd_{13}O_4$ with 8 CO molecules shows poor binding of the O_2 on the Mg sites with (E_b = 0.19 [0.21] eV), resulting in their desorption even at the lowest experimental temperatures. For instance, the bottom right panel of Figure 3b displays the cluster after the first O_2 has left its Mg site. The desorption of the last three O_2 (via the same mechanism) results in a $Pd_{13}O_4$ species with four CO molecules on corner bridge sites (E_b = 1.24 [1.03] eV) and four CO molecules on the first adlayer Pd top positions below the corner bridge sites (E_b = 1.03 [0.85] eV) as depicted in Figure 3c. Further CO decoration of Mg sites turned out to be energetically less favorable (E_b = 0.68 [0.53] eV), and therefore we consider the $Pd_{13}O_4(CO)_8$ in Figure 3c as the representative starting structure for the simulation of the subsequent type I TPD experiments.

For the type I process, we limit ourselves to consideration of Mars−van-Krevelen (MvK)-type[34] reaction mechanisms. In the MvK mechanism, the adsorbed CO molecules can react with the four oxygen atoms of the $Pd_{13}O_4$ core. For the first CO_2 formation, the CO on the corner bridge attacks one of the
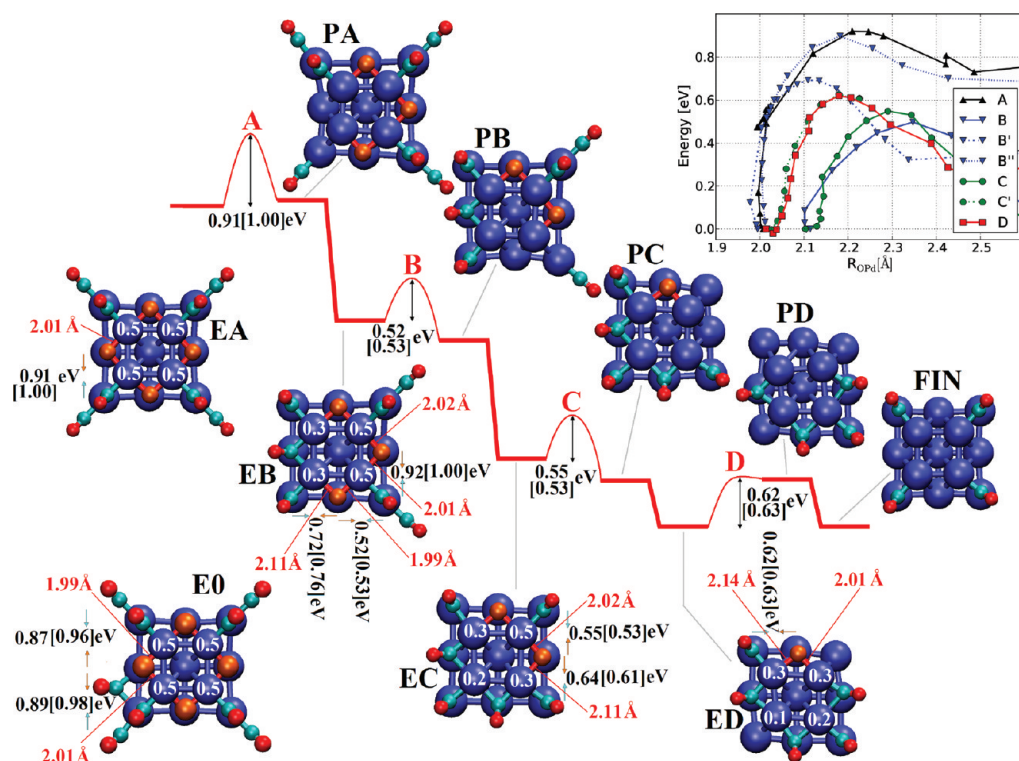
Figure 4. CO reacting with the $Pd_{13}O_4/MgO$. The red curve shows a schematic energy landscape of the reaction cascade consisting of four CO+O reaction steps. The structures EA–ED below the red curve are atomic optimal configurations of the reactant states for the reactions A–D. For clarity, the MgO support is not shown. The color code is the same as in Figure 3. White numbers represent the approximate Bader charges in the respective Pd atoms, black numbers the activation energies of the possible CO+O reactions (indicated by colored arrows), and the red numbers specify the length of the bonds connecting the O atoms with the neighboring Pd in the second layer of the cluster. The insets PA–PD and FIN above the red curve display the product states of the respective reaction. The inset in the upper right corner displays the various reaction pathways that start from reactant states EA–ED. The reaction coordinate ROPd is the distance between the reacting O and the second adlayer next nearest neighbor Pd atom that is not part of the reaction (i.e., the CO on the opposing corner bridge is oxidized during the reaction). Note that the curves look similar for the reactions with comparable barrier heights.

adjacent O atoms. The activation energy E_a = 0.91 [1.00] eV of this reaction is rather high (see reaction labeled A in the red curve of Figure 4, as well as the reactant and product state of this reaction displayed as insets EA and PA in Figure 4, respectively). As detailed below, it can be argued that the high symmetry of the $Pd_{13}O_4$ ground state underlies the observed higher reaction barrier height. Surprisingly, this symmetry is not significantly disturbed by an additional CO molecule adsorbed on a Pd–Pd bridge site above Mg (E_b = 0.68 [0.53] eV), because we still find the same barriers (~0.9 [1.0] eV) for CO_2 formation (inset E0 in the lower left corner of Figure 4). The reason for this fact is the relatively weak CO bonding; the CO desorbs before the first CO_2 molecule can be produced. This also justifies the choice of the C_{4v} structure as a starting configuration for the calculation of CO oxidation activation barriers. After desorption of the first CO_2, the vacant Pd–Pd corner bridge and Pd–Pd–Pd hollow positions (see PA in Figure 4) are spontaneously reoccupied by two CO molecules from the first adlayer Pd binding sites via a barrierless migration path. The resulting structure (EB in Figure 4) is the reactant state for the next reaction (B in the reaction path shown in Figure 4). Because of the broken C_{4v} symmetry, three different reactions with barriers ranging between 0.52 [0.53] and 0.92 [1.00] eV (indicated by the black numbers in EB Figure 4) occur on the C_{2v} $Pd_{13}O_3(CO)_7$. As the reaction rate for the process with the smallest activation energy is highest, we

assume that $Pd_{13}O_3(CO)_7$ takes the reaction channel with the 0.52 [0.53] eV barrier.

The vacant binding sites of the resulting product state (PB in Figure 4) are again filled by CO originating from first adlayer adsorptions sites. First, the CO on the bottom right corner of structure PB in Figure 4 moves upward to the Pd–Pd corner bridge. Next, the CO on the top right corner migrates along the right edge of the 9 atom bottom layer of the Pd_{13} followed by the passage around the Pd corner atom at the lower right corner of the Pd_{13} to a Pd–Pd bridge position. From there, the CO moves upward to its final position on the hollow site of the Pd_{13} side face. Surprisingly, all of these CO migration steps are essentially barrierless.

The resulting reactant state for reaction C is the C_{2v} $Pd_{13}O_2(CO)_6$ (EC in Figure 4). Here, only two reactions are possible with activation energies of 0.55 [0.53] and 0.64 [0.61] eV, respectively. The $Pd_{13}O(CO)_5$ product state (PC in Figure 4) produced by the E_a = 0.55 [0.53] eV reaction is only metastable and relaxes without barrier into structure ED in Figure 4. ED represents the reactant state of the last reaction (D in Figure 4) with a barrier of 0.62 [0.63] eV and a product state PD that transforms finally by a last CO rearrangement in a fully reduced C_{4v} $Pd_{13}(CO)_4$ (FIN in Figure 4).

The sequence of activation energies 0.91 [1.00] eV→0.52 [0.53] eV→0.55 [0.53] eV→0.62 [0.61] eV indicates that rather high temperatures (of the order of 400 K) are required to produce the first CO_2 accompanied by the immediate

formation of the remaining three CO_2. As was already mentioned, symmetry, and symmetry breaking, is likely to underlie the observed magnitude and range of variation of the activation energies. This conjecture is further corroborated by an analysis of structures and charge states of the reactants in Figure 4 (marked EA to ED). The C_{4v} reactant EA binds the O atoms with d = 2.01 Å bonds to the Pd atoms of the second layer of the cluster. The O atoms have a Bader charge of roughly −0.8 e, which originates mainly from the Pd atoms of the second adlayer (Bader charge of +0.5 e). After reaction A (product PA), the C_{4v} symmetry is broken and two types of O environments occur. The O atom at the right-hand-side edge of reactant EB retains its environment with the d = 2.01 Å bonds to the +0.5 e charged Pd atoms, and therefore it is not surprising that the CO_2 forming reaction with this O has still a high barrier of 0.92 [1.00] eV.

For the other two O atoms, a pronounced asymmetry occurs. One of the adjacent Pd atoms has reduced its Bader charge to +0.3 e (because it reduced its O coordination number during reaction A), resulting in an elongated Pd−O bond with d = 2.11 Å presumably due to the decreased Coulomb attraction between this Pd and the oxygen atom. Obviously, this asymmetry is responsible for the occurrence of two different barriers (∼0.5 and ∼0.7 eV), both being lower than the reaction barrier corresponding to the symmetric environment. Interestingly, the barrier for the reaction with CO on the more distant Pd atom (with d = 2.11 Å) is higher, suggesting that the stronger binding to the other Pd with d = 1.99 Å facilitates the corresponding CO+O reaction. The same trend can be observed for reactant EC where the same local environment leads to similar qualitative variation in the activation energies. Even for the last reaction, the remaining O is asymmetrically bonded via 2.14 and 2.01 Å bonds to the second layer Pd atoms. Because in this case no CO on the closer Pd−Pd corner bridge is available, the O has to react with the more remote CO, and therefore the barrier is higher as compared to reactions B and C.

The observed dependence of the reaction on the initial environment of the O atom can also be seen in the reaction pathways (inset in the upper right corner of Figure 4). If the distance ROPd between the reacting O and the Pd neighbor on the corner bridge (opposite to reacting CO) is used as a reaction coordinate, the curves with comparable barrier heights look similar and start at the same initial ROPd. This suggests that the reaction is initiated by the breaking of one Pd−O bond and that the barrier height is determined by the strength of this bond; that is, if this bond is short, it is hard to break, which results in a high barrier.

The strong binding of the four atomic oxygen in the second adlayer Pd_4O_4 square of the high-symmetry reactant state EA in Figure 4 can also be rationalized by an inspection of its electronic structure. Figure 5a displays the local density of electronic states (LDOS) of the oxygen atoms in the Pd_4O_4 square (red curve). The lowest unoccupied orbital (LUMO) and a series of orbitals below the highest occupied orbital (HOMO) have substantial weight on the Pd_4O_4 O atoms. These orbitals can be described as superpositions of atomic O(p) and Pd(d) type orbitals (see yellow/green isosurfaces, Figure 5a). The LUMO of EA exhibits a clear antibonding character for the O- and neighboring Pd-atoms, while all energetically lower lying occupied orbitals display bonding (HOMO−6, HOMO−5, HOMO−3) or mixed bonding/ antibonding (HOMO−2 and HOMO−1) character (except
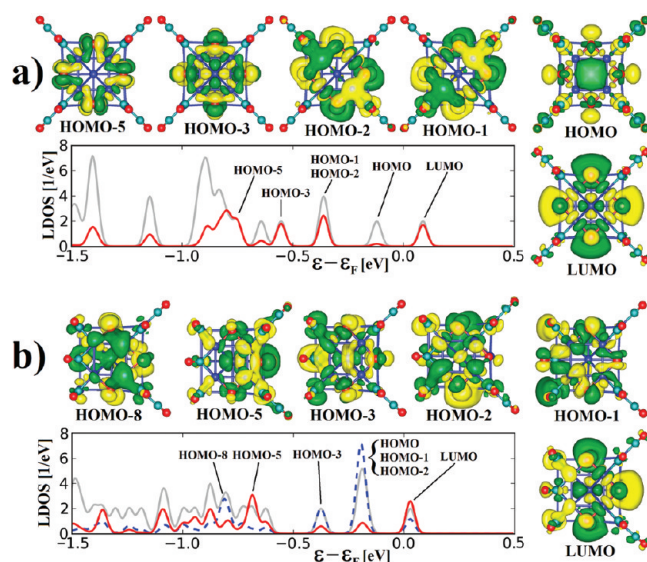

Figure 5. Spin-paired local density of electronic states (LDOS, broadened by 0.03 eV wide Gaussians) and selected electronic orbitals of the structures EA (panel a) and EB (panel b) of Figure 4. All energies are relative to the Fermi energy ε_F. Gray curves in both LDOS plots represent the total density of states (scaled by a factor 0.05). The LDOS values of the oxygen atoms in the second adlayer Pd_4O_x subsystem (x = 4 in EA and x = 3 in EB) are plotted as a red solid curve for O in a symmetric and a blue dashed curve for O in an asymmetric environment. The highest occupied molecular orbitals with significant LDOS on the Pd_4O_x oxygen atoms and the lowest unoccupied molecular orbital are displayed as yellow and green isosurfaces, where the two colors distinguish the sign of the wave functions. The color code for the atoms is the same as in Figure 3. Interestingly, the HOMO in panel a is of color-center-type; that is, it has substantial electronic density in the empty upper adlayer Pd_4 square.

the color-center-type HOMO that has no weight on the O atoms). These findings explain the strong bonds between the oxygen atoms and the Pd atoms that are obviously hard to break prior to the O+CO reaction.

The situation changes drastically when the symmetry of the upper Pd_4O_4 square is disturbed. The blue dashed curve in Figure 5b shows the LDOS of the two oxygen atoms in the second adlayer Pd_4O_3CO square of structure EB (Figure 4) with an asymmetric environment (reflected, for instance, by the different Bader charges on the neighboring Pd atoms; see Figure 4). The LDOS indicates that the binding of these two O atoms is determined by the HOMO−8, HOMO−3, HOMO− 2, and HOMO−1 (see corresponding orbital isosurfaces in Figure 5b). These orbitals are antibonding for both Pd−O bonds of the asymmetric oxygen atoms, except the HOMO-8 that is only antibonding for the long 2.11 Å Pd−O bond. The HOMO (not displayed) is again of color-center-type and has no significant weight on the O atoms in the second adlayer. The weakening of the d = 2.11 Å Pd−O bonds is also reflected in the LUMO, which shows bonding character for these bonds.

Interestingly, the O atom on the right-hand side of the Pd_4O_3CO square of EB in Figure 4 retains the same symmetry of the local environment as structure EA. The red curve in the LDOS (Figure 5b) indicates strong orbital weights on the LUMO and the HOMO−5. The striking similarity of the local structure of the LUMO on this atom and the LUMO of EA (Figure 5) as well as the bonding nature of the HOMO−5
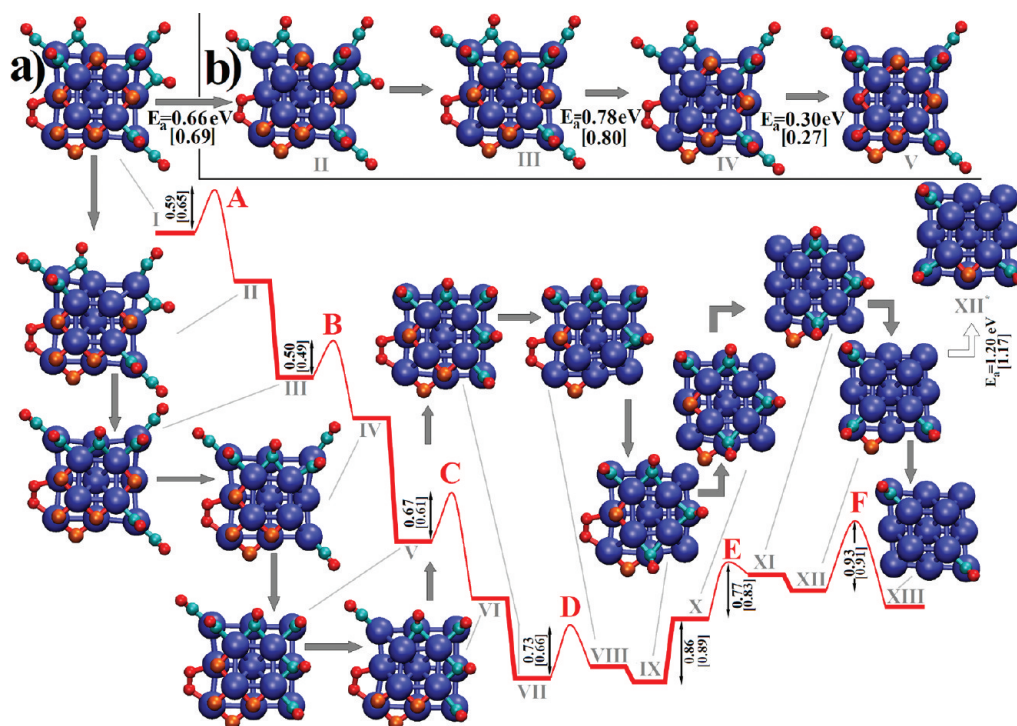
Figure 6. CO reactions with the $Pd_{13}O_6$/MgO. (a) Reaction pathway for the processes A−F with minimum activation energies for the CO+O reactions. The atomic configurations marked I−XIII in (a) show reactant and product states. Color code as in Figure 3. For clarity, the MgO support is not shown in the figure. Note that between IX and X the $^{18}O_2$ at the lower left of the cluster desorbs, because the smallest barrier of the alternative CO+O reaction is higher (0.92 eV) than the desorption energy (0.86 eV). Panel b displays an alternative reaction pathway that branches off from the start configuration I by a CO+O reaction with an insignificantly higher barrier (0.66 eV as compared to reaction A 0.59 eV). The sequence II−V in (b) depicts a possible pathway for dissociation of the $^{18}O_2$ at the lower left of the cluster. After the formation of structure V in (b), the usual CO+O reactions can continue, culminating with the formation of $C^{16}O^{18}O$.

provides further support to our previous conclusion that the local symmetry increases the bonding of the atomic O and consequently the barrier height for CO_2 formation.

To identify atomistic mechanisms underlying the TPD spectra of the type II experiments, we consider the $Pd_{13}O_6$ nanooxide in the bottom panel of Figure 2d resulting from the initial $^{16}O_2$ treatment at 370 K. As the clusters in the type II experiment were exposed to $^{18}O_2$ at 120 K afterward, we distinguish in the following between the two different O isotopes. Similar to the C_{4v} $Pd_{13}O_4$, the $Pd_{13}{}^{16}O_6$ nanooxide adsorbs $^{18}O_2$ on the corner bridge positions and on top of Mg. Because one corner bridge site is already occupied by a ^{16}O molecule, only the other three vacant corner bridges can be decorated by $^{18}O_2$. Furthermore, the occupation of one Mg site by another atomic ^{16}O impedes $^{18}O_2$ adsorption on the Mg site at one edge of the cluster. Therefore, the $Pd_{13}{}^{16}O_6$ cluster is decorated by six $^{18}O_2$ molecules after the 120 K dosing with this oxygen isotope. As in the C_{4v} $Pd_{13}O_4$ case, the subsequent low-temperature CO dosing leads to detachment of all corner bridge bonded $^{18}O_2$. Again, the oxygen dimers on the Mg sites are destabilized except for one $^{18}O_2$ that still binds with $E_b = 0.68$ [0.75] eV to a Mg site close to the ^{16}O on the Pd−Pd corner bridge. Figure 3d shows a top and side view of the final structure with full CO coverage (with orange color code for the six ^{16}O of the nanooxide).

Prior to discussion of the possible reaction mechanisms on this structure, we would like to address the stretch frequencies of the various $^{13}C^{16}O$ on this cluster and compare them with the experimental FTIR information (see inset in Figure 1). It is possible to weakly bind an additional vertically oriented $^{13}C^{16}O$

to the structure in Figure 3d (on the Mg atom below the ^{16}O on the Pd−Pd corner bridge, $E_b = 0.23$ [0.21] eV). We have performed a vibrational analysis of the resulting $Pd_{13}{}^{16}O_6{}^{18}O_2(^{13}C^{16}O)_7$, where the $^{13}C^{16}O$ bond lengths are stretched by 5% and the vibrational frequencies are determined through a subsequent isoenergetic molecular dynamics simulation.[35] In these calculations, the $^{13}C^{16}O$ on Pd−Pd bridge sites above the Mg atoms vibrate with a frequency $\nu = 1876$ cm^{-1}, $^{13}C^{16}O$ on the Pd−Pd corner bridges with $\nu = 1903-1916$ cm^{-1}, the $^{13}C^{16}O$ on top of the first layer cluster corner Pd atoms with $\nu = 2004-2008$ cm^{-1}, and for the $^{13}C^{16}O$ on top of the Mg atom at the oxidized corner bridge we find a vibrational frequency of 2016 cm^{-1}. This manifold of vibrational absorptions can well be related to the experimentally observed weak feature at around 2000 cm^{-1} and the relatively broad band at 1886 cm^{-1}. Note, however, that none of the calculated frequency agrees with the narrow experimental peak at 2068 cm^{-1}. This band might well originate from CO bound to nearby step edges and grain boundaries of the relatively small MgO terraces. Separate measurements of the MgO substrates without clusters at $T = 90$ K revealed frequencies of the order of 2140 cm^{-1}. Possibly, the presence of the clusters stabilizes these defect-bound CO molecules and shifts the frequency to lower wavenumbers.

The reduced symmetry of the $Pd_{13}{}^{16}O_6{}^{18}O_2(CO)_8$ suggests lower barriers for the first CO+O reaction than in the $Pd_{13}O_4$ C_{4v} case. Indeed, we find 0.59 [0.65] eV for the smallest activation energy for reaction A in Figure 6a. During this reaction and the following reactions B, C, and D with respective barriers 0.50 [0.49], 0.67 [0.61], and 0.73 [0.66] eV, the same

processes occur, as we already discussed for the C_{4v} case in Figure 4; that is, the reaction of the atomic O with a CO on a neighboring Pd−Pd corner bridge is followed by the migration of other CO molecules, leading to a reactant state for the subsequent reaction. Note that even the migration of an atomic O can take place on the $Pd_{13}O_6$ (compare structure VI to VII in Figure 6a), a process that was not observed on the C_{4v} $Pd_{13}O_4$.

After reaction D, all possible CO+O reactions would require an activation energy exceeding the binding energy of the still adsorbed $^{18}O_2$, which therefore desorbs before the next CO+O reaction, E, with a barrier of 0.77 [0.83] eV, occurs. After this reaction, all ^{16}O atoms in the second adlayer have been consumed, and only one ^{16}O atom remains on the cluster, located in the first adlayer on top of a Mg. Moving this ^{16}O to the second adlayer (resulting in structure XII* in Figure 5a) is kinetically hindered by a high activation energy of $E_a = 1.22$ [1.17] eV. A direct reaction of the neighboring CO on the corner bridge with the ^{16}O atom on the first adlayer site (reaction F in Figure 6a) has a lower activation energy of 0.93 [0.91] eV (corresponding to a ~400 K reaction temperature). The formation and desorption of the last CO_2 culminates in a fully reduced C_{2v} Pd_{13} with 2 CO on corner bridges.

There are also scenarios where the $^{18}O_2$ stays on the cluster until vacant sites in the second adlayer become available, with subsequent dissociation of this oxygen isotopomer. Figure 6b shows such a sequence. A CO+O reaction with a barrier of 0.66 [0.69] eV, leading to structure II in Figure 6b, represents a likely alternative to reaction A in Figure 6a. Structure III in Figure 6b results from the relaxation of the ^{16}O on the lower left corner bridge to an edge Pd hollow site and migration of CO to energetically more favorable positions (all of these processes entail activation energies $E_a < 0.3$ eV). A further CO +O reaction ($E_a = 0.78$ [0.80] eV) produces the structure marked IV in Figure 6, followed by the dissociation of the $^{18}O_2$ and the concurrent migration of two CO molecules ($E_a = 0.30$ [0.27] eV). Starting from the resulting structure V, reactions of the type $C^{16}O + {}^{18}O \rightarrow C^{16}O^{18}O$ lead to the formation of isotopically mixed carbon dioxide.

IV. DISCUSSION

The strong dependence of the TPD spectra on the details of the O_2 dosage is certainly the most striking finding from the experimental work (see Figure 1). The average higher reaction temperatures in type I experiments can be attributed to the milder oxidation conditions (no high-temperature O_2 pretreatment) that lead, according to the DFT study, to the formation of highly symmetric palladium nanooxides. The concomitant dissociation of oxygen at cryogenic temperatures and the formation of this stable nanooxide are surprising, particularly because for extended palladium surfaces and nanoparticles the dissociation of O_2 is often found to be the rate-determining step occurring at elevated temperatures (350−450 K). The formed highly symmetric species resists low-temperature MvK-type reactions. The width of the type I TPD spectra suggests, however, that not all clusters are of C_{4v} symmetry. Most likely a fraction of the nanooxides have reduced symmetry and consequently lower activation energies. The 370 K oxygen ($^{16}O_2$) pretreatment in type II experiments changes the TPD spectra drastically. Although the subsequent low-temperature $^{16}O_2$ and $^{13}C^{16}O$ dosages are comparable to the type I protocol, the type II TPD spectrum shifts to significantly smaller reaction temperatures. Our DFT results indicate that the harsher oxidation conditions (in the type II experiments) result in

nanooxides of lower symmetry, characterized by activation barriers for the CO combustion reaction that are markedly lower in comparison to those found for the reaction involving the C_{4v} nanooxide. The theoretical activation energies found for the CO combustion at the second adlayer of the cluster correlate with reaction temperatures in the range 250−300 K, underlying the assignment of these processes to the second maximum labeled β in the type II spectra displayed in Figure 1. Both $^{13}C^{16}O_2$ and $^{13}C^{16}O^{18}O$ contribute to this peak because under certain conditions molecularly adsorbed $^{18}O_2$ binds relatively strong to the nanooxide. As a consequence, during CO combustion and the concomitant reduction of the nanooxide, the $^{18}O_2$ molecule migrates to more reactive binding sites on the nanooxide and dissociates on the second layer to form strongly bound atomic ^{18}O that can be associated with the β-type reaction mechanism of the CO oxidation. The DFT calculations further suggest that the atomic ^{16}O bound at the first adlayer can be produced by the $^{16}O_2$ pretreatment at 370 K. The activation energy of the $^{13}C^{16}O_2$ formation of this species with corner bridge bonded $^{13}C^{16}O$ is significantly increased (~0.93 eV) and corresponds to reaction temperatures of the order of 400 K. This mechanism may explain the formation of carbon dioxide at highest temperature and labeled γ in the type II TPD data (Figure 1). This mechanism, allowing only the production of $^{13}C^{16}O_2$, also explains the absence of the γ peak in the $^{13}C^{16}O^{18}O$ partial TPD spectra.

In the DFT calculations, we focused on MvK-type reactions. The low-temperature peak marked α in the $C^{16}O^{18}O$ partial TPD spectra (see bottom of Figure 1) cannot be explained by this kind of reaction because dissociation of the $^{18}O_2$ is preceded by a series of higher temperature $^{13}C^{16}O_2$ reactions. Of course, a direct reaction of the $^{18}O_2$ with a neighboring $^{13}C^{16}O$ would be an alternative explanation for the observed α peak. We checked this possibility repeatedly for the reaction chain in Figure 6. In all cases, the barriers for such a Langmuir−Hinshelwood mechanism exceeded 1 eV, and, therefore, the α peak is unlikely to be produced by the $Pd_{13}O_6$ core considered in Figure 6. However, it cannot be excluded that the structure in Figure 6 coexists with a small fraction of other nanooxides that catalyze such a direct Langmuir−Hinshelwood type reaction. This conjecture is based on the small relative intensity of the α signal and the fact that its occurrence depends sensitively on the experimental conditions (i.e., the resulting nanooxide ensemble).

The joint experimental and theoretical work discussed here highlights the role of symmetry of the cluster, or cluster intermediate, in catalytic reactions. From the theoretical work, and the systematic correlation with the experimental findings, we conclude that the highly symmetric intermediates along the reaction path can increase the activation energy of subsequent reaction steps, in a substantial manner. Furthermore, low energy reaction channels may open subsequent to symmetry breaking. This concept seems also to be true for other cluster sizes. For example, for a larger cluster catalyst, Pd_{30}, supported on magnesia, whose ground state also reveals a C_{4v} symmetry,[36] we find behavior rather similar to that described by us here for the Pd_{13} cluster, with low-temperature CO combustion occurring, subsequent to breaking of the symmetry of the cluster−reactant complex. For the very small sizes, exhibiting structures of low symmetry (for example, Pd_8 supported on MgO), low-temperature reaction pathways were already observed without oxygen treatment.[37] This concept may also

apply to other systems, for example, enzymes, where the active centers often exhibit low-symmetry configurations.

■ ASSOCIATED CONTENT

ⓢ Supporting Information

Structures and energies of the minima shown in Figures 2−5. This material is available free of charge via the Internet at http://pubs.acs.org.

■ AUTHOR INFORMATION

Corresponding Author
michael.moseler@iwm.fraunhofer.de
Notes
The authors declare no competing financial interest.

■ ACKNOWLEDGMENTS

■ REFERENCES

(1) Cuenya, B. R. *Thin Solid Films* **2010**, *518*, 3127−3150.

(2) Croft, L. *Nat. Chem.* **2010**, *2*, 1009−1009.

(3) Gandhi, H. S.; Graham, G. W.; McCabe, R. W. *J. Catal.* **2003**, *216*, 433−442.

(4) Centi, G.; Ciambelli, P.; Perathoner, S.; Russo, P. *Catal. Today* **2002**, *75*, 3−15.

(5) Lundgren, E.; Kresse, G.; Klein, C.; Borg, M.; Andersen, J. N.; DeSantis, M.; Gauthier, Y.; Konvicka, C.; Schmid, M.; Varga, P. *Phys. Rev. Lett.* **2002**, *88*, 246103.

(6) Zemlyanov, D.; Aszalos-Kiss, B.; Kleimenov, E.; Teschner, D.; Zafeiratos, S.; Hävecker, M.; Knop-Gericke, A.; Schlögl, R.; Gabasch, H.; Unterberger, W.; Hayek, K.; Klötzer, B. *Surf. Sci.* **2006**, *600*, 983−994.

(7) Rogal, J.; Reuter, K.; Scheffler, M. *Phys. Rev. Lett.* **2007**, *98*, 046101.

(8) Rogal, J.; Reuter, K.; Scheffler, M. *Phys. Rev. B* **2008**, *77*, 155410.

(9) Gabasch, H.; Knop-Gericke, A.; Schlögl, R.; Borasio, M.; Weilach, Ch.; Rupprechter, G.; Penner, S.; Jenewein, B.; Hayek, K.; Klötzer, B. *Phys. Chem. Chem. Phys.* **2006**, *9*, 533−540.

(10) Schalow, T.; Brandt, B.; Starr, D. E.; Laurin, M.; Shaikhutdinov, S. K.; Schauermann, S.; Libuda, J.; Freund, H. J. *Angew. Chem., Int. Ed.* **2006**, *45*, 3693−3697.

(11) Nolte, P.; Stierle, A.; Kasper, N.; Jin-Phillipp, N. Y.; Reichert, H.; Rühm, A.; Okasinski, J.; Dosch, H. *Phys. Rev. B* **2008**, *77*, 115444.

(12) Huber, B.; Koskinen, P.; Häkkinen, H.; Moseler, M. *Nat. Mater.* **2006**, *5*, 44−47.

(13) Walter, M.; Moseler, M. *Phys. Status Solidi B* **2010**, *247*, 1016−1022.

(14) Abbet, S.; Judai, K.; Klinger, L.; Heiz, U. *Pure Appl. Chem.* **2002**, *74*, 1527−1535.

(15) Heiz, U.; Vanolli, F.; Trento, T.; Schneider, W. D. *Rev. Sci. Instrum.* **1997**, *68*, 1986−1994.

(16) Harding, C.; Habibpour, V.; Kunz, S.; Farnbacher, A. N.-S.; Heiz, U.; Yoon, B.; Landman, U. *J. Am. Chem. Soc.* **2009**, *131*, 538−548.

(17) Heiz, U.; Vanolli, U. F.; Trento, L.; Schneider, W.-D. *Rev. Sci. Instrum.* **1997**, *68*, 1986−1994.

(18) Abbet, S.; Riedo, E.; Brune, H.; Heiz, U.; Ferrari, A. M.; Giordano, L.; Pacchioni, G. *J. Am. Chem. Soc.* **2001**, *123*, 6172−6178.

(19) Di Valentin, C.; Del Vitto, A.; Pacchioni, G. *J. Phys. Chem. B* **2002**, *106*, 11961−11969.

(20) Mortensen, J. J.; Hansen, L. B.; Jacobsen, K. W. *Phys. Rev. B* **2005**, *71*, 035109.

(21) Enkovaara, J.; Rostgaard, C.; Mortensen, J. J.; Chen, J.; Dułak, M.; Ferrighi, L.; Gavnholt, J.; Glinsvad, C.; Haikola, V.; Hansen, H. A.; Kristoffersen, H. H.; Kuisma, M.; Larsen, A. H.; Lehtovaara, L.; Ljungberg, M.; Lopez-Acevedo, O.; Moses, P. G.; Ojanen, J.; Olsen, T.; Petzold, V.; Romero, J. A.; Stausholm-Møller, N.; Strange, M.; Tritsaris, G. A.; Vanin, M.; Walter, M.; Hammer, B.; Häkkinen, H.; Madsen, G. K. H.; Nieminen, R. M.; Nørskov, J. K.; Puska, M.; Rantala, T. T.; Schiøtz, J.; Thygesen, K. S.; Jacobsen, K. W. *J. Phys.: Condens. Matter* **2010**, *22*, 253202.

(22) Perdew, J. P.; Burke, K.; Ernzerhoft, M. *Phys. Rev. Lett.* **1996**, *77*, 3865−3868.

(23) Tao, J.; Perdew, J. P.; Staroverov, V. N.; Scuseria, G. E. *Phys. Rev. Lett.* **2003**, *91*, 146401.

(24) Perdew, J. P.; Tao, J.; Staroverov, V. N.; Scuseria, G. E. *J. Chem. Phys.* **2004**, *120*, 6898.

(25) Bitzek, E.; Koskinen, P.; Gahler, F.; Moseler, M.; Gumbsch, P. *Phys. Rev. Lett.* **2006**, *97*, 170201.

(26) Henkelmann, G.; Johnson, H. *J. Chem. Phys.* **2000**, *113*, 9978.

(27) Henkelman, G.; Uberuaga, B. P.; Jónsson, H. *J. Chem. Phys.* **2000**, *113*, 9901.

(28) Kanai, Y.; Wang, X.; Seloni, A.; Car, R. *J. Chem. Phys.* **2006**, *125*, 234104.

(29) Graoui, H.; Giorgio, S.; Henry, C. R. *Philos. Mag. B* **2001**, *81*, 1649−1658.

(30) Moseler, M.; Häkkinen, H.; Barnett, R. N.; Landman, U. *Phys. Rev. Lett.* **2001**, *86*, 2545−2548.

(31) Bader, R. W. F. *Atoms in Molecules: A Quantum Theory*; Oxford University Press: New York, 1990.

(32) Tang, W.; Sanville, E.; Henkelman, G. *J. Phys.: Condens. Matter* **2009**, *21*, 084204.

(33) Campbell, C. T.; Sun, Y.-K.; Weinberg, W. H. *Chem. Phys. Lett.* **1991**, *179*, 53−57.

(34) Mars, P.; van Krevelen, D. W. *Chem. Eng. Sci.* **1954**, *3*, 41−59.

(35) Yoon, B.; Landman, U.; Wörz, A. S.; Antonietti, J. M.; Abbet, S.; Judai, K.; Heiz, U. *Science* **2005**, *307*, 403−407.

(36) Yoon, B.; Landman, U.; Habipour, V.; Harding, C.; Kunz, S.; Heiz, U.; Moseler, M.; Walter, M. *J. Phys. Chem. C*, dx.doi.org/10.1021/jp301314s.

(37) Heiz, U.; Sanchez, A.; Abbet, S.; Schneider, W.-D. *Chem. Phys.* **2000**, *262*, 189−200.